Phys Chem Minerals (2017) 44:109–123
DOI 10.1007/s00269-016-0841-6

ORIGINAL PAPER

Spinel and post-spinel phase assemblages in Zn_2TiO_4: an experimental and theoretical study

Yanyao Zhang[1,2] · Xi Liu[1,2] · Sean R. Shieh[3] · Xinjian Bao[1,2] · Tianqi Xie[3] · Fei Wang[1,2] · Zhigang Zhang[4] · Clemens Prescher[5] · Vitali B. Prakapenka[5]

Received: 23 May 2016 / Accepted: 4 September 2016 / Published online: 16 September 2016

Abstract Zn_2TiO_4 spinel (Zn_2TiO_4-Sp) was synthesized by a solid-state reaction method (1573 K, room *P* and 72 h) and quasi-hydrostatically compressed to ~24 GPa using a DAC coupled with a synchrotron X-ray radiation (ambient *T*). We found that the Zn_2TiO_4-Sp was stable up to ~21 GPa and transformed to another phase at higher *P*. With some theoretical simulations, we revealed that this high-*P* phase adopted the $CaTi_2O_4$-type structure (Zn_2TiO_4-CT). Additionally, the isothermal bulk modulus (K_T) of the Zn_2TiO_4-Sp was experimentally obtained as 156.0(44) GPa and theoretically obtained as 159.1(4) GPa, with its first pressure derivative K_T' as 3.8(6) and 4.37(4), respectively. The volumetric and axial isothermal bulk moduli of the Zn_2TiO_4-CT were theoretically obtained as K_T = 150(2) GPa (K_T' = 5.4(2); for the volume), $K_{T\text{-}a}$ = 173(2) GPa ($K_{T\text{-}a}'$ = 3.9(1); for the *a*-axis), $K_{T\text{-}b}$ = 74(2) GPa ($K_{T\text{-}b}'$ = 7.0(2); for the *b*-axis), and $K_{T\text{-}c}$ = 365(8) GPa ($K_{T\text{-}c}'$ = 1.5(4); for the *c*-axis), indicating a strong elastic anisotropy. The Zn_2TiO_4-CT was found as ~10.0 % denser than the Zn_2TiO_4-Sp at ambient conditions. The spinel and post-spinel phase assemblages for the Zn_2TiO_4 composition at high *T* have been deduced as Zn_2TiO_4-Sp, $ZnTiO_3$-ilmenite + ZnO-wurtzite, $ZnTiO_3$-ilmenite + ZnO-rock salt, $ZnTiO_3$-perovskite + ZnO-rock salt, and Zn_2TiO_4-CT as *P* increases, which presumably implies a potential stability field for a CT-type Mg_2SiO_4 at very high *P*.

Keywords Compressibility · DFT calculations · Diamond-anvil cell · High-*P* phase transition · Synchrotron X-ray diffraction · Zn_2TiO_4-CT · Zn_2TiO_4-Sp

Introduction

The common phase for the composition Zn_2TiO_4 is a 4–2 inverse spinel (Zn_2TiO_4-Sp; Verwey and Heilmann 1947), which has wide technological applications as white-color pigment, sorbent material, dielectric resonator, photocatalyst, refractory material, and photoluminescent material and has attracted a lot of attention (e.g., Grigoryan and Grigoryan 2001; Souza et al. 2005; Chaves et al. 2006; Rankin et al. 2008; Borse et al. 2012; Chen 2012). In Earth sciences, the Zn_2TiO_4-Sp phase is conventionally considered as a low-*P* analogue of the Mg_2SiO_4 spinel (Millard et al. 1995; Wang et al. 2002), the most abundant mineral in the lower part of the mantle transition zone (Ringwood and Reid 1968; Irifune and Ringwood 1987; Ita and Stixrude 1992; Frost 2008), so that its high-*P* behavior may shed light on our understanding about the high-*P* behavior of the Mg_2SiO_4 composition. Existing investigations have suggested that for the Mg_2SiO_4 composition, the stable phase assemblages are forsterite (Fo), wadsleyite (Wd), ringwoodite (spinel-type Mg_2SiO_4 termed as Mg_2SiO_4-Sp hereafter), bridgmanite (perovskite-type $MgSiO_3$ termed

✉ Xi Liu
xi.liu@pku.edu.cn

1 Key Laboratory of Orogenic Belts and Crustal Evolution, MOE, Peking University, Beijing 100871, People's Republic of China

2 School of Earth and Space Sciences, Peking University, Beijing 100871, People's Republic of China

3 Department of Earth Sciences, University of Western Ontario, London, ON N6A 5B7, Canada

4 Key Laboratory of Earth and Planetary Physics, Institute of Geology and Geophysics, Chinese Academy of Sciences, Beijing 100029, People's Republic of China

5 Center for Advanced Radiation Sources, University of Chicago, Chicago, IL 60439, USA

as $MgSiO_3$-Pv hereafter) + periclase (rock salt-type MgO termed as MgO-Rs hereafter), and post-perovskite ($MgSiO_3$-PPv) + MgO-Rs as pressure increases from the surface to the core–mantle boundary of the Earth (Ringwood and Major 1966; Suito 1972; Liu 1976; Ito 1977; Murakami et al. 2004; Oganov and Ono 2004; Tsuchiya et al. 2004). What phase assemblage this composition attains at still higher pressures is currently largely unknown due to the present unavailability of highly reliable experimental techniques at multimegabar pressures, which, however, may have important application to the extrasolar planets with masses up to 10 times that of the Earth (Valencia et al. 2006; Swift et al. 2012; Wagner et al. 2012). In this respect lies the interest of the current study about the high-*P* behavior of the composition Zn_2TiO_4.

Although the high-*P* behavior of the Zn_2TiO_4 composition is potentially very useful, inadequate effort has been paid on this topic so far. At ambient *P*, this composition forms two substances, one adopting a tetragonal structure (space group $P4_122$) and stable at low *T* while the other attaining a cubic structure (space group $Fd\bar{3}m$) and stable at high *T*, with their phase transition *T* in the range of 763–833 K due to some possible but inadequately characterized reasons such as small compositional difference and slow phase transition rate between these two phases (Delamoye et al. 1970; Millard et al. 1995). The cubic form is in fact the 4–2 inverse Zn_2TiO_4-Sp. At ambient *T*, some in situ X-ray diffraction and Raman spectroscopic data suggested that the Zn_2TiO_4-Sp is stable up to ~23.7 GPa and transforms to an orthorhombic phase with the $CaTi_2O_4$-type structure at higher *P* (Zn_2TiO_4-CT; space group *Cmcm*; Wang et al. 2002). No much experimental data about the composition Zn_2TiO_4 exist at simultaneously high-*P* and high-*T* conditions.

The 4–2 inverse Zn_2TiO_4-Sp is cubic and has the space group $Fd\bar{3}m$ (no. 227; $Z = 8$). Its ideal structural formula can be written as $\left(Zn^{2+}\right)^{tet}\left[Zn^{2+}Ti^{4+}\right]^{oct}O_4$, with the oxygen atoms in an approximately close-packed *fcc* structure (equipoint 32*e*), the Zn^{2+} cations on both the tetrahedral sites (8*a*) and octahedral sites (16*d*), and the Ti^{4+} cations on the octahedral sites only. It is well known that upon compression the Sp structure may attain some isochemical denser structures such as the $CaFe_2O_4$-type structure [CF; space group *Pnma*, e.g., $MgAl_2O_4$-Sp vs. $MgAl_2O_4$-CF (Irifune et al. 1991)], the $CaMn_2O_4$-type structure [CM; space group *Pbcm*, e.g., Fe_3O_4-Sp vs. Fe_3O_4-CM (Fei et al. 1999)], and the CT structure [e.g., Zn_2TiO_4-Sp vs. Zn_2TiO_4-CT (Wang et al. 2002)], the ε-$MgAl_2O_4$-type structure [e.g., $MgAl_2O_4$-Sp vs. $MgAl_2O_4$-ε (Liu 1978; Ono et al. 2006)], and the tetragonal distorted structure with the space group $I4_1/amd$ [TDS; $ZnGa_2O_4$-Sp vs. $ZnGa_2O_4$-TDS (Errandonea et al. 2009) and $MgCr_2O_4$-Sp vs. $MgCr_2O_4$-TDS (Yong et al. 2012)]. It is also well known that alternatively, the Sp phase may break down at high *P* to some new phase assemblages such as Rs + Ilm (ilmenite-type phase) (e.g., Mg_2TiO_4-Sp → MgO-Rs + $MgTiO_3$-Ilm; Akimoto and Syono 1967), and Rs + Ru (rutile-type phase) (e.g., Mg_2SnO_4-Sp → MgO-Rs + SnO_2-Ru; Ringwood and Reid 1968). In the case of the Zn_2TiO_4-Sp, preliminary high-*P* experimental data at room *T* suggested a Zn_2TiO_4-CT phase at $P >$ ~23.7 GPa, which is ~2.1 % denser than the Zn_2TiO_4-Sp at ambient *P*–*T* condition (Wang et al. 2002). Considering the absence of any pressure medium in the reported diamond-anvil cell (DAC) experiments (Wang et al. 2002), and the strong similarity of the powder X-ray diffraction patterns of the CT, CF, and CM structures (Yamanaka et al. 2008), more investigation on the high-*P* behavior of the Zn_2TiO_4 composition is deemed necessary.

In this study, we have synthesized the Zn_2TiO_4-Sp using a solid-state reaction method (ambient *P*), quasi-hydrostatically compressed this material to ~24 GPa using a DAC coupled with a synchrotron X-ray radiation (ambient *T*), and found that the Zn_2TiO_4-Sp is stable up to ~21 GPa and transforms to another phase at higher *P*. In order to determine the structure of this high-*P* phase, we have conducted some theoretical simulations and found that this phase adopts the CT structure. In addition, the compressional behaviors of the Zn_2TiO_4-Sp and Zn_2TiO_4-CT have been investigated and compared. Furthermore, we have tentatively deduced the spinel and post-spinel phase assemblages for the Zn_2TiO_4 composition at high-*P* and high-*T* conditions, and preliminarily discussed the possibility of an Mg_2SiO_4-CT phase at very high pressures.

Experimental and simulating methods

The Zn_2TiO_4-Sp was synthesized by a conventional solid-state reaction method at 1573 K and 1 atm. We used the chemicals ZnO (99.99 %, Alfa Aesar) and TiO_2 (99.99 %, Alfa Aesar) to prepare the starting material for the high-*T* synthesizing experiment. We firstly dried these chemicals at 1 atm and 1373 K for 36 h, secondly weighed them according to the stoichiometry of the Zn_2TiO_4-Sp and homogenized them into a mixture with an agate mortar under acetone, and thirdly pressed this mixture into a pellet. This pellet was placed in a platinum crucible and sintered with a muffle furnace in open air. The sample was heated at 1573 K for 72 h and then slowly cooled to room *T* at the rate of −5 K/min. According to Dulin and Rase (1960), our synthetic product was expected to be pure Zn_2TiO_4-Sp.

One part of the synthetic sample from the high-*T* synthesizing experiment was processed and characterized by using a scanning electron microscope (Quanta 650 FEG) and an electron microprobe (EMP; JEOL JXA-8100). The other part of the sample was slowly ground down to a fine

powder, which was first checked with a powder X-ray diffractometer (X'Pert Pro MPD system) at ambient *P*–*T* conditions, and later used in our high-*P* synchrotron X-ray diffraction experiments.

Our high-*P* synchrotron X-ray diffraction experiments (ambient *T*) were conducted with a symmetrical DAC at the beamline 13-ID-D of the GSECARS, Advanced Photon Source (APS), Argonne National Laboratory. The experimental techniques were similar to those used in our previous studies (e.g., Liu et al. 2011; He et al. 2012). The powder sample, mixed with a trace amount of Au powder, was loaded into a rhenium gasket with a hole of 100 μm in diameter. Some other experimental details included: neon used as the pressure medium, a ruby sphere as the pressure marker (the ruby fluorescence method; Mao et al. 1978), and an incident synchrotron radiation beam monochromatized to the wavelength of 0.3344 Å and collimated to the beam size of ~3×4 μm^2. The sample-to-detector distance (246.4524 mm) and the orientation of the detector were calibrated by using LaB_6. Each X-ray diffraction image was collected for about 30–120 s using an online CCD detector, and later integrated to derive the one-dimensional X-ray diffraction pattern by using the Dioptas program (Prescher and Prakapenka 2015). The XRD data were processed by using the PeakFit V4.12 software (SPSS Inc.), and the unit-cell parameters were obtained by using the UnitCell program (Holland and Redfern 1997).

Our first-principles simulations were completed with the CASTEP code using density functional theory (DFT; Hohenberg and Kohn 1964; Kohn and Sham 1965) and planewave pseudopotential technique (Payne et al. 1992). For the Zn_2TiO_4-Sp, we carefully examined different exchange–correlation potentials and pseudopotentials for some different initial structures (more discussion later), and eventually chose an ordered 1 × 1×1 conventional cell ($Z = 8$) with the lowest energy reported by Rankin et al. (2008) as the initial structure for our simulation. On the other hand, the initial structural models of the Zn_2TiO_4-CT, Zn_2TiO_4-CM, and Zn_2TiO_4-CF were from Bertaut and Blum (1956), Giesber et al. (2001), and Decker and Kasper (1957), respectively. We treated the exchange–correlation interaction by generalized gradient approximation (GGA) with the Perdew–Burker–Ernzerhof functional (PBE; Perdew et al. 1996), and used a convergence criterion of 10^{-6} eV/atom on the total energy in the self-consistent field calculations. We employed the ultrasoft pseudopotential to model the ion–electron interaction, and the planewave basis set with a cutoff of 380 eV to expand the electronic wave functions (Vanderbilt 1990; Kresse and Hafner 1994). We sampled the irreducible Brillouin zone with 2 × 2×2, 2 × 5×1, 5 × 1×2, and 1 × 1×5 Monkhorst–Pack grids (Monkhorst and Pack 1976) for the Zn_2TiO_4-Sp, Zn_2TiO_4-CF, Zn_2TiO_4-CM, and Zn_2TiO_4-CT, respectively. The effects of using larger cutoff and k point meshes on the calculated properties were found to be insignificant. The equilibrium lattice parameters, internal coordinates, and internal energies at different pressures were optimized by minimizing the Hellmann–Feynman force on the atoms and simultaneously matching the stress on the unit cell to the target stress.

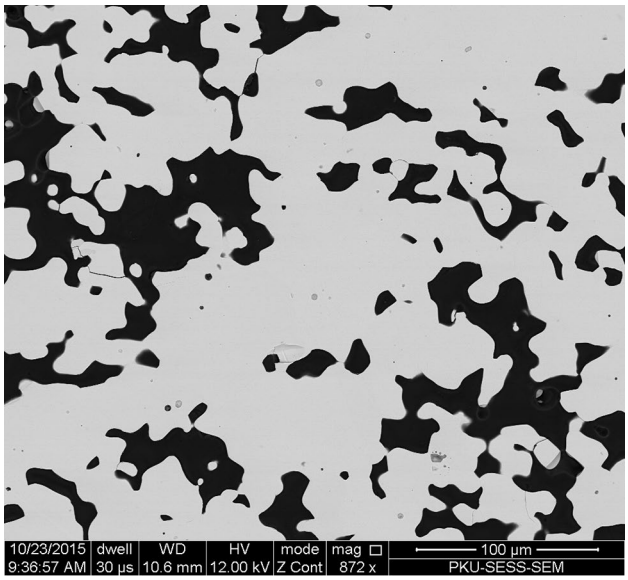

Fig. 1 Electron backscatter image of synthetic Zn_2TiO_4-Sp. The bright material is Zn_2TiO_4-Sp, whereas the dark material is epoxy

Result and discussion

Synthetic Zn_2TiO_4-Sp: composition and unit-cell parameter variation

The electron backscatter images of our synthetic product suggest that there is only one crystalline phase, with grain sizes ranging from a few micrometers to a few dozens of micrometers (Fig. 1). The powder X-ray diffraction data indicate no impurity and confirm the expected cubic spinel structure. In contrast, previous effort synthesizing single Zn_2TiO_4-Sp phase with the solid-state reaction method at much lower *T* (e.g., 873–1273 K; Bartram and Slepetys 1961) was only partially successful and persistently generated the phase assemblage Zn_2TiO_4-Sp + ZnO.

The EMP analyses (7 analyses) performed on our synthetic product suggest a chemical formula of $Zn_{1.92(0)}Ti_{1.04(1)}O_{4.00}$, indicating the cation substitution mechanism $2Zn^{2+} = Ti^{4+}$ and the presence of a small amount of cation vacancy (~ 1.3 %). This phenomenon is in obvious contrast to our stoichiometric Mg_2TiO_4-Sp synthesized at even higher *T* (1673 K) with similar experimental

techniques (Lv et al. 2016). Zinc has a relatively high vapor pressure which increases with T, so that the zinc vacancy in our Zn_2TiO_4-Sp might readily form at high temperatures due to the loss of ZnO by volatility (Dulin and Rase 1960; Nikolić et al. 2008). In this study, we assume that the effect of this small amount of non-stoichiometry on the physical–chemical properties of the Zn_2TiO_4-Sp is negligible, despite that it may become somewhat prominent as the extent of the non-stoichiometry becomes very significant (e.g., the difference in the isothermal bulk moduli (K_T) of the spinels $MgAl_2O_4$ and $Mg_{0.4}Al_{2.4}O_4$ is as large as ~11.5 %; Nestola et al. 2009).

The powder X-ray diffraction data at ambient conditions give out the unit-cell parameters of our Zn_2TiO_4-Sp synthesized at 1573 K as $a_0 = 8.472(2)$ Å and $V_0 = 608.17(39)$ Å^3, in good agreement with Bartram and Slepetys (1961; $a_0 = 8.471(2)$ Å; synthesizing $T = 1473$ K) and Millard et al. (1995; $a_0 = 8.46948(2)$ Å; synthesizing $T = 1483$ K), but in relatively poor agreement with Wang et al. (2002; $a_0 = 8.4562(11)$ Å; synthesizing $T = 1473$ K). Since all the investigated samples were synthesized with the solid-state reaction method at similar temperatures and were expected to be broadly similar in chemical compositions and microscopic structure features (e.g., order–disorder status and cation vacancy), the difference in the unit-cell parameters between Wang et al. (2002) and all other studies may presumably reflect the difference in the setups of the X-ray diffraction experiments. According to Fleet et al. (2010; Table 5), different setups in the XRD experiments may lead to significant difference in the unit-cell parameters for the same material under investigation. Alternatively, the unit-cell parameters may be affected by the exact distribution of the Zn and Ti cations on the tetrahedral and octahedral sites of the Zn_2TiO_4-Sp, an order–disorder phenomenon well known for the spinel structure. With the equations in Hazen and Yang (1999) and the tetrahedra and octahedral cation–oxygen bond distances from Shannon (1976; an oxygen radius of 1.38 Å assumed), the unit-cell parameters of the fully inverse Zn_2TiO_4-Sp and normal Zn_2TiO_4-Sp are roughly approximated as $a_0 = 8.5136$ and $a_0 = 8.4244$ Å, respectively. Similar to the Mg_2TiO_4-Sp, the Zn_2TiO_4-Sp should be a completely ordered inverse 4–2 spinel at low T, and become gradually disordered as T increases (O'Neill et al. 2003), so that its unit-cell parameters are expected to be negatively correlated with the synthesizing T. Indeed, this correlation was observed by Bartram and Slepetys (1961): As the calcination T increased from 1173 to 1673 K, the parameter a was reduced by ~0.002 Å, indicating an extremely small amount of Zn and Ti redistribution on the tetrahedral and octahedral sites. It follows that the order–disorder factor should have a negligible effect on the unit-cell parameters of the Zn_2TiO_4-Sp.

The unit-cell parameters of the synthetic Zn_2TiO_4-Sp prepared by different experimental methods such as the solid-state reaction method, the polymeric precursor method, the high-energy ball milling method, and the thermal oxidation method showed very large variation. The solid-state reaction method is the conventional method, and the resulting samples have their a_0 parameters ranging from ~8.445 to 8.477 Å (e.g., Verwey and Heilmann 1947; Bartram and Slepetys 1961; Wang et al. 2002). As the T-dependent order–disorder phenomenon is not an important issue, we must resort to potential compositional difference in the synthetic materials. Despite early powder XRD investigation conducted by Dulin and Rase (1960) concretely ruled out any extensive solid solution behavior for the Zn_2TiO_4-Sp, our direct EMP data clearly demonstrated the possibility of some compositional deviation from the stoichiometry, which might have been the case indeed due to different sintering temperatures, durations, and oxygen fugacities employed in those synthesizing experiments. In some cases, the solid-state reaction method was combined with low-T hydrogen–oxygen plasma or high-energy planetary milling, which might have promoted the formation rate of the Zn_2TiO_4-Sp and led to much better stoichiometry and almost constant unit-cell parameter [$a_0 = \sim 8.471$–8.474 Å, essentially identical to our observed value; Grigoryan and Grigoryan (2001), Nikolić et al. (2008)]. The polymeric precursor method is relatively new and usually generates synthetic phases with high stoichiometric precision. The a_0 parameter of the Zn_2TiO_4-Sp synthesized with this method is relatively smaller (~8.440–8.463 Å; Souza et al. 2005; Chaves et al. 2006; Santos et al. 2009), presumably indicating a good stoichiometry of the synthetic product. The high-energy ball milling method and thermal oxidation method were recently employed to produce the Zn_2TiO_4-Sp in a nanocrystalline form (e.g., Manik et al. 2003; Santhaveesuk et al. 2008). Perhaps because of the lattice imperfections in the nanostructure, the a_0 values are generally larger (~8.474–8.480 Å).

High-P behavior of Zn_2TiO_4-Sp: compression experiments

Our compression experiments (ambient T) were conducted up to ~24 GPa. The X-ray diffraction patterns obtained at pressures up to ~20.6 GPa did not show any apparent peak-broadening, peak-splitting, or new peak (Fig. 2), suggesting no phase transition up to this pressure. However, the X-ray diffraction pattern collected at ~22 GPa showed significant peak-broadening and attained some new peaks which could not be attributed to the cubic spinel structure. It follows that there must have been a phase transition somewhere between ~20.6 and 22 GPa, a phenomenon in general agreement with Wang et al. (2002; the phase transition

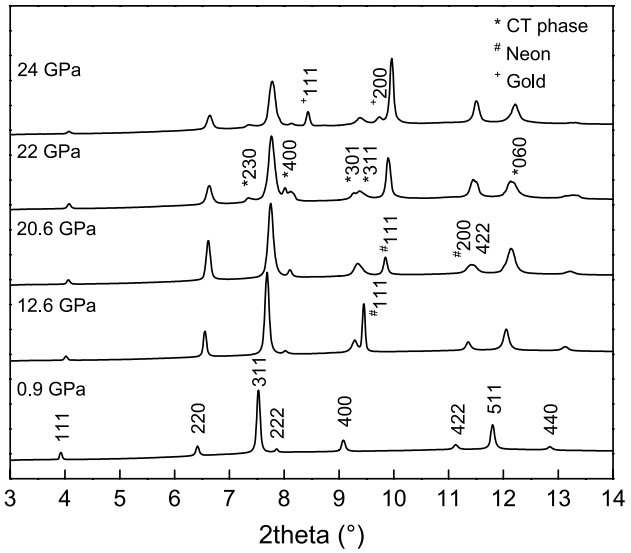

Fig. 2 XRD patterns collected at 0.9, 12.6, 20.6, 22, and 24 GPa (ambient *T*). All major peaks can be assigned to Zn_2TiO_4-Sp, with small peaks belonging to Zn_2TiO_4-CT, neon or gold. The X-ray peaks of Zn_2TiO_4-CT become evident at 22 GPa

pressure claimed as ~23.7 GPa). On the other hand, the major peaks of the X-ray diffraction pattern collected at ~24 GPa can be confidently assigned to the Zn_2TiO_4-Sp still, indicating an incompletion of the phase transition. Wang et al. (2002) observed the completion of the phase transition at ~32.4 GPa.

The experimentally obtained unit-cell parameters of the Zn_2TiO_4-Sp at different pressures are summarized in Table 1 and shown in Fig. 3. Clearly, the data at $P >$ ~15 GPa show some deviation from the trend defined by the data at lower pressures. Since the magnitude of this deviation is positively correlated with the experimental *P*, we tend to ascribe it to the progressive development of a non-hydrostatic condition in our DAC experiments. According to Klotz et al. (2009), our pressure medium, neon, becomes incapable maintaining a quasi-hydrostatic environment at $P >$ ~15 GPa.

In order to accurately determine the K_T of the Zn_2TiO_4-Sp, the *P*–*V* data collected at pressures from 1 atm to 15 GPa are fitted with the third-order Birch–Murnaghan equation of state (BM-EoS; Birch 1947) by a least-squares method:

$$P = 3K_T f_E(1+2f_E)^{\frac{5}{2}}\left[1+\frac{3}{2}(K_T^{'}-4)f_E\right], \quad (1)$$

where $K_T^{'}$ is the first pressure derivative of K_T, and f_E is the Eulerian definition of finite strain ($[(V_0/V)^{2/3}-1]/2$). In the Eulerian definition of the finite strain, V_0 is the volume at zero pressure, whereas *V* is the volume at high

Table 1 Experimental unit-cell parameters of Zn_2TiO_4-Sp at various pressures (room *T*)

P (GPa)	*a* (Å)	*V* (Å^3)
0.0001	8.472(2)[b]	608.17(39)
0.9(1)[a]	8.449(2)	603.18(48)
1.7(1)	8.440(2)	601.25(39)
2.0(1)	8.437(2)	600.65(38)
2.3(1)	8.429(2)	598.92(33)
2.7(1)	8.423(2)	597.66(38)
3.1(1)	8.416(2)	596.15(38)
3.7(1)	8.407(2)	594.19(38)
4.3(1)	8.396(2)	591.96(41)
4.8(1)	8.388(2)	590.15(38)
5.1(1)	8.386(2)	589.66(38)
5.6(1)	8.377(2)	587.92(37)
6.4(1)	8.363(2)	584.81(37)
7.0(1)	8.349(2)	582.01(37)
8.0(1)	8.338(2)	579.74(37)
9.0(1)	8.327(2)	577.48(40)
10.0(1)	8.314(2)	574.70(40)
11.0(1)	8.299(2)	571.50(39)
11.5(1)	8.289(2)	569.50(39)
12.6(1)	8.273(2)	566.27(36)
13.5(1)	8.260(2)	563.56(35)
14.1(1)	8.251(2)	561.63(35)
15.0(1)	8.243(2)	560.06(35)
15.5(1)	8.232(2)	557.89(35)
16.5(1)	8.226(2)	556.67(35)
17.0(1)	8.222(2)	555.76(35)
18.0(1)	8.216(2)	554.61(35)
18.4(1)	8.212(3)	553.75(60)
19.2(1)	8.205(2)	552.29(40)
20.6(1)	8.195(3)	550.35(59)
22.0(1)	8.184(2)	548.07(39)
24.0(1)	8.167(2)	544.81(42)

[a] *P* determined by averaging the values measured before and after collection of synchrotron data; uncertainty of *P* in the high-*P* experiments assumed as 0.1 GPa

[b] Numbers in parentheses representing 1 SD

pressure. When $K_T^{'}$ is set as 4, we obtain $K_T = 154.6(12)$ GPa, and $V_0 = 607.86(20)$ Å^3 for the Zn_2TiO_4-Sp. If $K_T^{'}$ is not fixed, we obtain $K_T = 156.0(44)$ GPa, $K_T^{'} = 3.8(6)$ and $V_0 = 607.79(29)$ Å^3.

The quality of the derived third-order BM-EoS for the Zn_2TiO_4-Sp can be evaluated by using the f_E-*F* plot (Fig. 4); *F* is defined as $F \equiv P/[3f_E(1+2f_E)^{5/2}]$. Using *F*, the third-order BM-EoS can be rewritten as:

$$F = K_T + 3/2K_T(K_T^{'}-4)f_E, \quad (2)$$

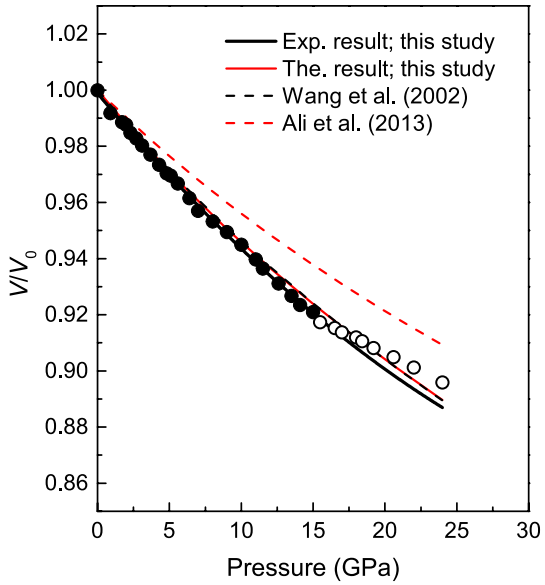

Fig. 3 Pressure dependence of normalized volume (V/V_0) for Zn_2TiO_4-Sp (ambient T). The experimental data collected at pressures up to ~15 GPa and at pressures higher than ~15 GPa are represented by *filled* and *empty circles*, respectively (*error bars* equal to or smaller than the size of the *symbols*). The *solid black curve* is drawn according to our third-order BM-EoS ($V_0 = 608.17(39)$ Å^3; see text for the details). In comparison, the experimental result from Wang et al. (2002) is shown as the *broken black curve* ($V_0 = 604.68(24)$ Å^3). Additionally, our simulating result as represented by the *solid red curve* ($V_0 = 626.95$ Å^3) is compared to that from the theoretical work of Ali et al. (2013; the *broken red curve*; $V_0 = 601.21$ Å^3)

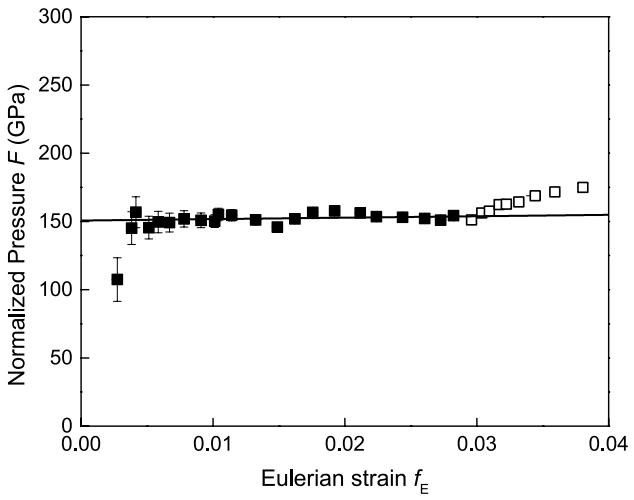

Fig. 4 Eulerian strain-normalized pressure (f_E-F) plot for Zn_2TiO_4-Sp. Estimated standard deviations have been calculated following the method in Heinz and Jeanloz (1984). Experimental data in the P ranges of below and above 15 GPa are represented by *filled* and *empty squares*, respectively. The *solid* nearly *horizontal line* represents a weighted linear fit through the data in the P range from 1 atm to ~15 GPa

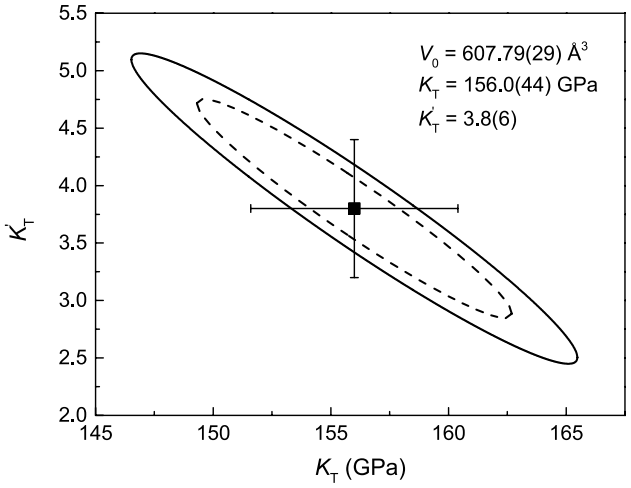

Fig. 5 Confidence ellipse in K_T and $K_T^{'}$ confirming our P-V data fit for Zn_2TiO_4-Sp. The *inner ellipse* and *out ellipse* are for a 68.3 % confidence level (χ^2 distribution with 2 degrees of freedom $\Delta = 2.30$; see Angel (2000) for details) and a 90 % confidence level ($\Delta = 4.61$), respectively. The K_T and $K_T^{'}$ values obtained by the least-squares refinement (the software EoS fit 5.2; Angel 2000) are also shown. *Error bars* correspond to $\pm 1\sigma$

so that the slope of the line defined by the experimental data should be equal to 3/2 K_T ($K_T^{'}-4$), and the intercept value is the isothermal bulk modulus. Figure 4 shows that the slope of the fitted line for the data in the P range from 1 atm to ~15 GPa is fairly close to zero so that the value of the $K_T^{'}$ should be about 4, confirming our EoS fit. Additionally, Fig. 4 shows that the data at $P >$ ~15 GPa gradually deviate away from the nearly horizontal line defined by the data at lower pressures, indicating that the spinel structure was increasingly strained due to the progressive development of the non-hydrostatic pressure environment in our DAC experiments at $P >$ ~15 GPa (Klotz et al. 2009).

In order to evaluate the correlation between the K_T and $K_T^{'}$ obtained with our compressional data from 1 atm to 15 GPa, a series of confidence ellipses in the K_T-$K_T^{'}$ space have been constructed (Bass et al. 1981; Fig. 5). The ellipses strongly elongate with negative slopes, reflecting a negative correlation between the K_T and $K_T^{'}$ parameters. It follows that the experimental data can be fitted almost equally well by decreasing the value of K_T and increasing the value of $K_T^{'}$, or vice versa. In Fig. 5, the area enclosed by the dashed line or solid line represents a 68.3 % or 90 % probability (or confidence level; Angel 2000) that the true values of K_T and $K_T^{'}$ lie in such an area, respectively. If we consider the 90 % confidence ellipse, the K_T value can vary in the range from ~146 to 165 GPa with the $K_T^{'}$ value from ~5.1 to 2.4, which then justifies our data fitting process.

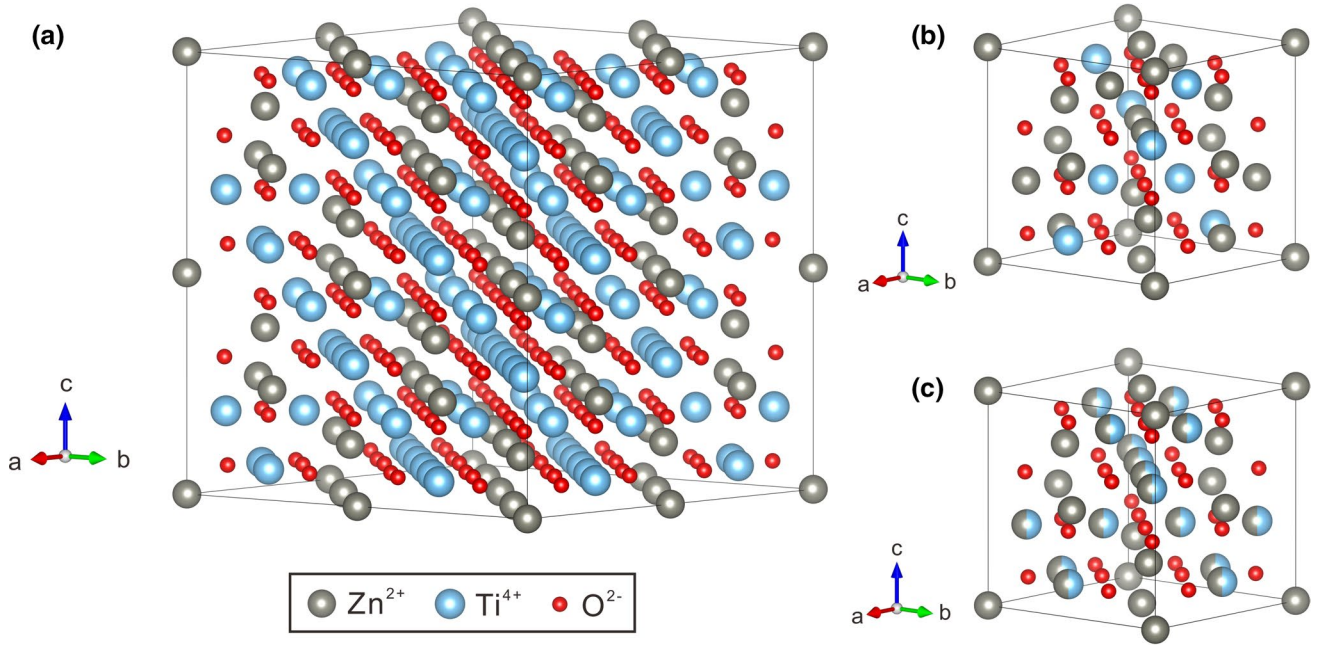

Fig. 6 Three candidate configurations as initial structures of Zn_2TiO_4-Sp for DFT calculations. **a** One of the 2 × 2 × 2 supercells ($Z = 64$) with $F\bar{4}3m$ space group; **b** one of the 1 × 1 × 1 convention cells ($P4_122$ space group) with lowest energy according to Rankin et al. (2008); **c** the structure constructed by VCA method, with each atom in the octahedral sites composed of half Zn^{2+} cation and half Ti^{4+} cation

Initial structure of Zn_2TiO_4-Sp for DFT calculations

In order to perform DFT calculations for the Zn_2TiO_4-Sp, it is necessary to know the atomic positions of the Ti^{4+} and Zn^{2+} cations on the octahedral sites, which unfortunately could not be determined by X-ray diffraction techniques (Bartram and Slepetys 1961; Rankin et al. 2008). The behavior of cationic disorder on the octahedral sites of the Zn_2TiO_4-Sp may be investigated by several computational approaches. One direct but usually expensive approach is to study all ordered supercells, followed by configurational averaging or finding out the lowest energy configuration, so that the local chemical environment can be accurately probed (e.g., Rankin et al. 2008; Deng et al. 2011). Another simpler and less expensive approach is the virtual crystal approximation (VCA; Nordheim 1931), which assumes that on each disordered site there is a "virtual" atom averaging the behaviors of the actual components, and thus ignores any possible short-range order (e.g., Bellaiche and Vanderbilt 2000; Ramer and Rappe 2000). Another approach is the "computational alchemy" method (e.g., de Gironcoli et al. 1991), which uses the perturbation theory to calculate the response to the difference between the true and VCA potentials, and is computationally demanding. Other approaches such as the coherent potential approximation and special quasi-random structure method may be employed (Soven 1967; Zunger et al. 1990; Wei and Zhang 2001).

We used two methods, the supercell and VCA, to constrain the structure of the Zn_2TiO_4-Sp. One of the 2 × 2 × 2 supercells ($Z = 64$) is displayed in Fig. 6a with the space group $F\bar{4}3m$, which has the highest symmetry, is the closest to the true structure among the various configurations of the 2 × 2 × 2 supercells, but is very expensive from a computational point of view. For simplicity, 1 × 1 × 1 convention cells ($Z = 8$) can be simulated with a reasonable computational cost. Since there exist 12,870 ($16!/8!^2$) configurations for the different occupations of the octahedral sites in the lattice with either Ti^{4+} or Zn^{2+} cations (Rankin et al. 2008), it is not practically possible to use the DFT to calculate the energies of all possible configurations. Rankin et al. (2008) chose 21 configurations to optimize their structures, including some high-symmetry configurations, low-symmetry configurations, configurations that pair Zn^{2+}–Zn^{2+} and Ti^{4+}–Ti^{4+} cations in the octahedral rows, and two random configurations. Among them, one of the lowest energy structures with no Zn^{2+}–Zn^{2+} and Ti^{4+}–Ti^{4+} pairs in close proximity is displayed in Fig. 6b. This configuration has the space group $P4_122$ (no. 91, $Z = 4$), and its lattice parameters are: $a = a'/\sqrt{2}$, $b = a'/\sqrt{2}$, and $c = a'$, where a' is the lattice parameter of the cubic spinel structure. Figure 6c shows the Zn_2TiO_4-Sp structure constructed

Table 2 Optimized crystallographic data with different combinations of configuration, exchange–correlation potential, and pseudopotential for Zn_2TiO_4-Sp

#	V_0 (Å^3)	RD[a]	u_0^b	RD[a]	Technique details[c]
1	626.95	3.14	–	–	Cc/GGA/usp
2	580.60	−4.48	–	–	Cc/LDA/usp
3	663.12	9.09	–	–	Cc/GGA/ncp
4	613.53	0.93	–	–	Cc/LDA/ncp
5	533.21	−12.28	0.3913	3.24	VCA/GGA/usp
6	492.40	−19.00	0.3921	3.45	VCA/LDA/usp
7	598.03	−1.62	0.3937	3.88	VCA/GGA/ncp
8	557.29	−8.32	0.3932	3.76	VCA/LDA/ncp

[a] Relative difference (%) between theoretical result and Bartram and Slepetys (1961; $V_0 = 607.86(43)$; $u_0 = 0.379$[b])

[b] The oxygen parameter, reflecting the exact positions of the oxygens. For an ideal cubic close-packing of oxygens in the spinel, u is 0.375 if the unit-cell origin is set at −0.125, −0.125, −0.125 from the center of symmetry (Hill et al. 1979)

[c] Technique details listed in the order of configuration (Cc, the 1 × 1×1 convention cell in Fig. 6b; VCA, the structure in Fig. 6c), exchange–correlation potential (GGA and LDA), and pseudopotential (*usp* ultrasoft pseudopotential, *ncp* norm-conserving pseudopotential)

by using the VCA method, with all atoms on the octahedral sites consisting of half Zn^{2+} and half Ti^{4+} cations.

The lattice parameters were optimized for the two chosen configurations (Fig. 6b, c) using different exchange–correlation potentials [GGA or local density approximation (LDA)] and different pseudopotentials (ultrasoft or norm-conserving) at zero pressure. In total, eight sets of lattice parameters have been obtained, as summarized and compared with the experimental results of Bartram and Slepetys (1961) in Table 2. Table 2 suggests that three combinations, namely #1, #4, and #7, reproduce the experimental unit-cell volume reasonably well, with relative differences of 3.14, 0.93, and −1.62 %, respectively. Since the LDA method usually underestimates the unit-cell volumes of the spinels (Rodríguez-Hernández and Muñoz 2014; Zhang et al. 2016), the combination #4 which overestimates in this case may be relatively inappropriate. Moreover, the optimized u_0 of the VCA cell with the combination #7 is significantly overestimated (Table 2), so that this combination may be discarded as well. Eventually, the combination #1 has been chosen to forward our DFT calculations, with the 1 × 1 × 1 conventional cell shown in Fig. 6b as the initial structure for the Zn_2TiO_4-Sp.

Structure of post-spinel phase and its unit-cell parameters

Our compression experiments have revealed that for the Zn_2TiO_4 composition, a phase transition from the

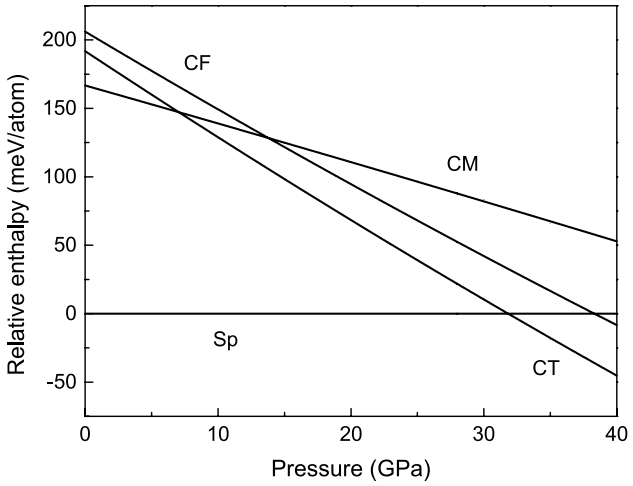

Fig. 7 Calculated enthalpies of the Sp, CM, CF, and CT phases (Zn_2TiO_4) relative to the enthalpy of the Sp for the P range of 0–40 GPa

Table 3 Experimentally observed XRD peaks compared with calculated major XRD peaks of Zn_2TiO_4-CT at 22 GPa

h	k	l	d_{obs} (Å)	d_{calc} (Å)	$d_{obs} - d_{calc}$ (Å)
0	2	0	–	4.7105	–
1	0	1	–	2.6249	–
2	3	0	2.6038	2.6240	−0.0202
1	1	1	–	2.5286	–
4	0	0	2.3929	2.3882	0.0047
1	2	1	–	2.2929	–
3	0	1	2.0709	2.0724	−0.0015
3	1	1	2.0255	2.0240	0.0015
3	2	1	–	1.8971	–
3	3	1	–	1.7298	–
0	6	0	1.5732	1.5702	0.0030
1	5	1	–	1.5307	–
5	2	1	–	1.4855	–
6	3	0	–	1.4201	–

The unit-cell parameters at 22 GPa were obtained as $a = 9.553(6)$ Å, $b = 9.421(3)$ Å, $c = 2.730(2)$ Å, and $V = 245.66(18)$ Å^3

Zn_2TiO_4-Sp to a new phase initiates at ~21 GPa, in general agreement with Wang et al. (2002). According to Wang et al. (2002), this new phase may adopt the CT structure (Zn_2TiO_4-CT). Since the X-ray data from Wang et al. (2002) were taken under severely non-hydrostatic pressure condition, the structural assignment of this phase needs to be further examined.

Our compression experiments were conducted up to ~24 GPa only, a pressure much lower than that for the completion of this phase transition (~32.4 GPa; Wang et al. 2002), so that only a few relatively weak X-ray peaks not

Table 4 Calculated unit-cell parameters of Zn_2TiO_4-Sp and Zn_2TiO_4-CT at various pressures (GPa) and zero *T*

Zn_2TiO_4-Sp			Zn_2TiO_4-CT					
P	*V* (Å^3)	V/V_0	*P*	*a* (Å)	*b* (Å)	*c* (Å)	*V* (Å^3)	V/V_0
0	626.95	1.000	0	9.9880	10.0830	2.8277	284.78	1.000
3	615.66	0.982	5	9.8962	9.8996	2.8151	275.79	0.968
6	605.35	0.966	10	9.8146	9.7658	2.8032	268.68	0.943
9	595.92	0.951	15	9.7386	9.6590	2.7896	262.40	0.921
12	587.25	0.937	20	9.6739	9.5711	2.7782	257.23	0.903
15	579.19	0.924	25	9.6087	9.4904	2.7667	252.30	0.886
18	571.57	0.912	30	9.5497	9.4226	2.7556	247.96	0.871
21	564.50	0.900	35	9.4967	9.3658	2.7427	243.95	0.857
24	557.79	0.890	40	9.4436	9.3102	2.7324	240.24	0.844

Table 5 Isothermal bulk moduli of Zn_2TiO_4-Sp and Zn_2TiO_4-CT and their phase transition pressure[a]

Zn_2TiO_4-Sp		Zn_2TiO_4-CT								P_T	Method[b]	References
K_T	K_T'	$K_{T\text{-}a}$	$K_{T\text{-}a}'$	$K_{T\text{-}b}$	$K_{T\text{-}b}'$	$K_{T\text{-}c}$	$K_{T\text{-}c}'$	K_T	K_T'			
156.0(44)	3.8(6)	–	–	–	–	–	–	–	–	~21	Exp/SX/Ne	This study
154.6(12)	4[c]	–	–	–	–	–	–	–	–	~21	Exp/SX/Ne	This study
162(11)	4[c]	–	–	–	–	–	–	205(6)	4[c]	~23.7	Exp/SX/No	Wang et al. (2002)
159.1(4)	4.37(4)	173(2)	3.9(1)	74(2)	7.0(2)	365(8)	1.5(4)	150(2)	5.4(2)	~32	The/DFT/GGA + PBE/usp	This study
162.9(5)	4[c]	170(0)	4[c]	110(5)	4[c]	312(6)	4[c]	171(3)	4[c]	~32	The/DFT/GGA + PBE/usp	This study
198.74	5.0	–	–	–	–	–	–	–	–	–	The/DFT/GGA + mBJ/fp	Ali et al. (2013)
207.8(8)	4[c]	–	–	–	–	–	–	–	–	–	The/DFT/GGA + mBJ/fp	Ali et al. (2013)

[a] P_T, phase transition pressure (GPa); K_T and K_T', volumetric isothermal bulk modulus (GPa) and its pressure derivative, respectively; $K_{T\text{-}a}$ and $K_{T\text{-}a}'$ ($K_{T\text{-}b}$ and $K_{T\text{-}b}'$, and $K_{T\text{-}c}$ and $K_{T\text{-}c}'$), axial isothermal bulk modulus (GPa) and its pressure derivative, respectively

[b] Some technique details: *Exp* experimental, *The* theoretical, *SX* synchrotron X-ray, *Ne* pressure medium of neon, *No* no pressure medium, *DFT* density functional theory, *GGA + PBE* generalized gradient approximation with Perdew–Burker–Ernzerhof functional, *GGA + mBJ* generalized gradient approximation with modified Becke–Johnson exchange potential, *usp* ultrasoft pseudopotentials, *fp* full potential scheme

[c] Fixed value

attributable to the Zn_2TiO_4-Sp were observed (Fig. 2). Consequently, the exact structure of this new phase could not be fully constrained by our X-ray data. As discussed earlier, a number of structures, including the CF, CM, CT, $MgAl_2O_4$-ε, and TDS types, are possible candidates. Our X-ray data could rule out the $MgAl_2O_4$-ε- and TDS-type structures due to the absence of their most intense X-ray lines, but could not tell which one of the CF, CM, and CT structures is the correct answer. These three structures have very similar powder XRD patterns (Yamanaka et al. 2008).

Theoretical simulation has been proved to be an effective method for determining the relative stabilities of different polymorphs, and thus employed in this study. The calculated enthalpies of the CF, CM, and CT structures relative to that of the Sp structure for the *P* range of 0–40 GPa are shown in Fig. 7. Obviously, the Zn_2TiO_4-Sp has the lowest enthalpy from 0 to ~32 GPa, whereas the Zn_2TiO_4-CT has the lowest enthalpy at higher *P*. It follows that the new phase observed in our high-*P* experiments highly possibly adopts the CT structure, in consistent with the interpretation in Wang et al. (2002).

The experimentally observed X-ray diffraction peaks for the Zn_2TiO_4-CT at 22 GPa have been summarized in Table 3, evidently supporting the assignment of the CT structure to the new high-*P* phase. With a Rietveld analysis, we obtained for the Zn_2TiO_4-CT at 22 GPa the following unit-cell parameters: $a = 9.553(6)$ Å, $b = 9.421(3)$ Å, $c = 2.730(2)$ Å, and $V = 245.66(18)$ Å^3. Similarly, we obtained its unit-cell parameters at 24 GPa as $a = 9.523(6)$ Å, $b = 9.378(3)$ Å, $c = 2.724(2)$ Å, and $V = 243.26(18)$ Å^3. The derived *a*:*b*:*c* ratio is thus 3.499(3):3.451(3):1 at 22 GPa or 3.496(3):3.443(3):1 at 24 GPa, which is significantly different to that of 3.007(1):2.958(1):1 at 32.4 GPa from Wang et al. (2002). This difference is largely caused by the very small compressibility of the *c*-axis compared to that of the *a*- or *b*-axis (more discussion later).

EoS of Zn_2TiO_4-Sp and Zn_2TiO_4-CT: theoretical results

The high-P unit-cell parameters of the Zn_2TiO_4-Sp predicted by our first-principles calculation are listed in Table 4: As P increases from zero pressure to 24 GPa, the unit-cell volume decreases from 626.948 to 557.785 Å^3 (by 11.03 %). Fitting these data with Eq. (1), we obtain $K_T = 159.1(4)$ GPa, $K_T^{'} = 4.37(4)$ and $V_0 = 626.92(4)$ Å^3, or $K_T = 162.9(5)$ GPa and $V_0 = 626.6(1)$ Å^3 ($K_T^{'} = 4$) for the Zn_2TiO_4-Sp, in excellent agreement with our experimental determinations (Table 5).

The theoretically constrained correlation between the normalized volume and pressure is compared in Fig. 3 with our experimentally obtained result, along with the results from earlier investigations (Wang et al. 2002; Ali et al. 2013). Compared to our experimental result, the curve obtained with our DFT calculations has slightly smaller slope, implying a slightly larger K_T (162.9(5) GPa vs. 154.6(12) GPa on the basis of $K_T^{'} = 4$). Nominally, the experimental result from Wang et al. (2002) seems in excellent agreement with our theoretical result, as indicated by the overlapping of the two representing curves shown in Fig. 3. Since there was no any pressure medium in their DAC experiments, their result born relatively large uncertainty ($K_T = 162(11)$ GPa if $K_T^{'}$ is fixed as 4), in strong comparison with our experimental result (154.6(12) GPa). On the other hand, the theoretical result from Ali et al. (2013) is very different to all other results (Fig. 3). Their K_T value, 207.8(8) GPa (with $K_T^{'}$ fixed as 4), is about 34.4(13) or 27.6(8) % larger than our experimentally or theoretically determined result, respectively. As discussed earlier, the octahedral sites in the Zn_2TiO_4-Sp structure are randomly filled by equal amounts of Zn^{2+} and Ti^{4+} cations, leading to a huge number of possible cation configurations (Rankin et al. 2008). Unfortunately, these different local arrangements of the Zn^{2+} and Ti^{4+} cations in the octahedral sites result in significantly different total energies and lattice parameters in the DFT calculations (Rankin et al. 2008; Rodríguez-Hernández and Muñoz 2014). Despite the fact that Ali et al. (2013) did not provide any details about their treatment of the distributions of the Zn^{2+} and Ti^{4+} cations in the octahedral sites, the sharp difference between their result and our result strongly suggests that the arrangements of the Zn^{2+} and Ti^{4+} cations can significantly affect the K_T of the Zn_2TiO_4-Sp as well. One minor but potential complication to this interpretation is that the inadequately reported setting parameters in the DFT calculations of Ali et al. (2013) may affect the calculated K_T value somewhat (Zhang et al. 2016).

The high-P unit-cell parameters of the Zn_2TiO_4-CT predicted by our first-principles calculation are listed in Table 4 and shown in Fig. 8. All unit-cell parameters vary non-linearly with P for the investigated P range from 1 atm to 40 GPa, with the a-axis decreasing from 9.9880 to 9.4436 Å (by 5.45 %), the b-axis from 10.0830 to 9.3102 Å (by 7.66 %), the c-axis from 2.8277 to 2.7324 Å (by 3.37 %), and the volume from 284.775 to 240.238 Å^3 (by 15.64 %).

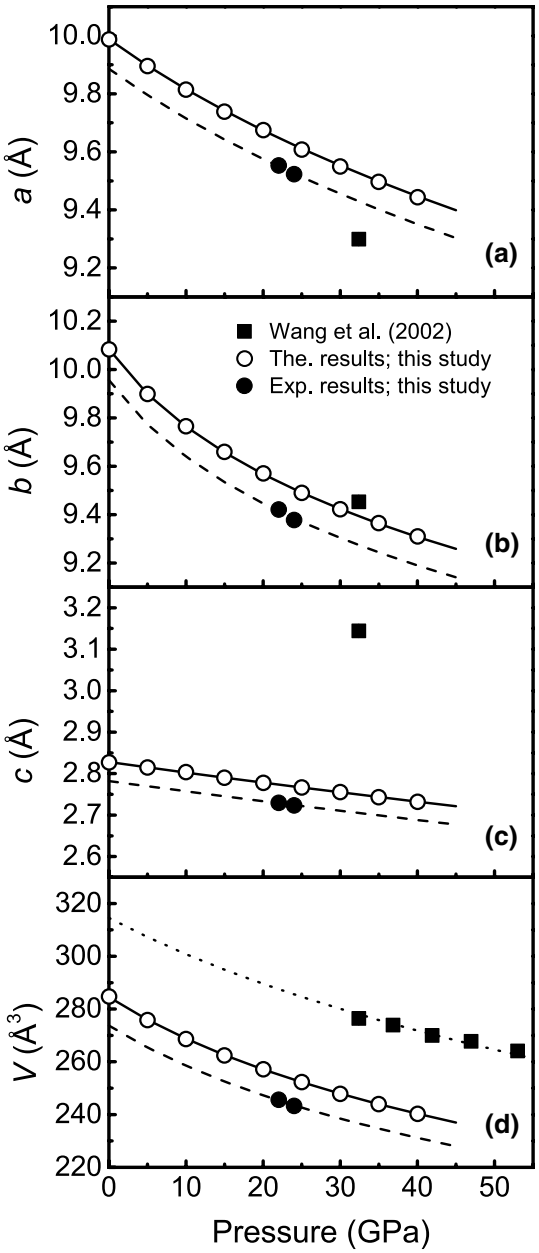

Fig. 8 Unit-cell parameters of Zn_2TiO_4-CT at high pressures obtained in our DFT calculation: **a** the a-axis; **b** the b-axis; **c** the c-axis; **d** the volume. The *solid black curves* are drawn according to our third-order BM-EoS parameters. In addition, the two experimental data at ~22 and 24 GPa are also plotted. Note that the *broken curves* drawn through the experimental data share the same K_T ($K_{T\text{-}a}$, $K_{T\text{-}b}$, $K_{T\text{-}c}$) and $K_T^{'}$ ($K_{T\text{-}a}^{'}$, $K_{T\text{-}b}^{'}$, $K_{T\text{-}c}^{'}$) but different V_0 (a_0, b_0, c_0) with the *solid curves*. For comparison, the experimental data from Wang et al. (2002) are also plotted. The *dotted curve* in **d** is drawn according to the BM-EoS from Wang et al. (2002)

Table 6 Spinel and post-spinel phase assemblages in Zn_2TiO_4 and Mg_2SiO_4 at high P and high T

Phase assemblage	Zn_2TiO_4	Mg_2SiO_4
Sp	Yes	Yes
Ilm + Wz	Yes	No
Ilm + Rs	Yes	No
Pv + Rs	Yes	Yes
PPv + Rs	No	Yes
CT	Yes	?

Sp spinel-type phase, *Ilm* ilmenite-type phase, *Wz* wurtzite-type phase, *Rs* rock salt-type phase, *Pv* perovskite-type phase, *PPv* post-perovskite-type phase, *CT* $CaTi_2O_4$-type phase

The calculated P–V data for the Zn_2TiO_4-CT have been fitted to Eq. (1), yielding $V_0 = 284.6(2)$ Å^3, $K_T = 150(2)$ GPa and $K_T^{'} = 5.4(2)$, or $V_0 = 283.5(4)$ Å^3 and $K_T = 171(3)$ GPa if $K_T^{'}$ is fixed as 4. Compared to our predicted K_T and V_0 values for the Zn_2TiO_4-Sp on the basis of $K_T^{'} = 4$, the K_T value for the Zn_2TiO_4-CT is about 5(2) % larger, whereas the V_0 value is about 9.5(1) % smaller (see Tables 5, 4, respectively). On the other hand, our theoretically estimated K_T value for the Zn_2TiO_4-CT is much small than the experimentally obtained K_T value by Wang et al. (2002; 205(6) GPa). Two factors possibly made their contributions: one was the lacking of experimental measurements at low pressures which usually leads to a poor EoS fit (note the experimental P range in Wang et al. 2002; Fig. 8d), and the other was the non-hydrostatic pressure in the DAC experiments without any pressure medium which commonly leads to an overestimated K_T when the sample is probed by an X-ray beam positioned parallel to the loading direction of the DAC (Fei 1999).

A linearized third-order Birch–Murnaghan equation of state (Angel 2000) has been used to obtain the parameters of the equations of state for the crystallographic axes of the Zn_2TiO_4-CT, yielding $a_0 = 9.988(1)$ Å, $K_{T\text{-}a} = 173(2)$ GPa and $K_{T\text{-}a}^{'} = 3.9(1)$ for the a-axis, $b_0 = 10.084(5)$ Å, $K_{T\text{-}b} = 74(2)$ GPa and $K_{T\text{-}b}^{'} = 7.0(2)$ for the b-axis, and $c_0 = 2.8278(5)$ Å, $K_{T\text{-}c} = 365(8)$ GPa and $K_{T\text{-}c}^{'} = 1.5(4)$ for the c-axis. It follows that the Zn_2TiO_4-CT has a prominent elastic anisotropy ($K_{T\text{-}a}$:$K_{T\text{-}b}$:$K_{T\text{-}c}$ = 2.3:1:4.9), with the b-axis as the most compressible axis and the c-axis as the least compressible one.

The very strong elastic anisotropy of the Zn_2TiO_4-CT might have had a complicated role in the experiments of Wang et al. (2002). When compressed in a DAC under severely non-hydrostatic condition, the Zn_2TiO_4-CT could be structurally distorted, or even show lattice preferred orientation with its (010) plane normal to the compression axis of the DAC (Miyajima et al. 2010). The combined effect of the non-hydrostatic stress distribution in the DAC and strong elastic anisotropy of the Zn_2TiO_4-CT may explain the slightly smaller value for the a-axis but larger values for the b- and c-axes observed by Wang et al. (2002), as compared to our results shown in Fig. 8.

In order to eliminate potential systematic difference between the experimental and the theoretic results, we have tentatively derived some new equations of state for the Zn_2TiO_4-CT by combining our theoretically calculated volumetric and axial isothermal bulk moduli, with our experimentally determined unit-cell parameters at ~22 and 24 GPa (Fig. 8). Eventually, we obtained $a_0 = 9.886$ Å, $b_0 = 9.956$ Å, $c_0 = 2.782$ Å, and $V_0 = 273.7$ Å^3 for the Zn_2TiO_4-CT at ambient P–T conditions. The Zn_2TiO_4-CT is thus ~10.0 % denser than the Zn_2TiO_4-Sp at ambient conditions, significantly different to the ~2.1 % density difference suggested by Wang et al. (2002).

Spinel and post-spinel phase assemblages at high P and high T

No experiments have been performed with the Zn_2TiO_4 composition at simultaneously high-P and high-T conditions so far. However, some experimental data exist for the compositions of Mg_2TiO_4, Fe_2TiO_4, and Co_2TiO_4 (Akimoto and Syono 1967): At P < ~1–4 GPa and high T like 1473 K, the stable phase assemblage for these three compositions is the Mg_2TiO_4-Sp, Fe_2TiO_4-Sp, and Co_2TiO_4-Sp, respectively; at higher P, these titanate spinels all break down to the phase assemblage of $MTiO_3$ + MO (M = Mg, Fe, and Co, respectively), with the $MTiO_3$ phase attaining the Ilm structure and the MO phase adopting the Rs structure. As the Zn_2TiO_4 composition also takes the cubic spinel structure at ambient P and similar T such as 1473 K (Delamoye et al. 1970; Millard et al. 1995), it seems reasonable to postulate that the Zn_2TiO_4-Sp similarly breaks down to the phase assemblage $ZnTiO_3$-Ilm + ZnO-Rs at P > ~1–4 GPa and high temperatures. Existing experimental studies have indicated that at 1473 K for example, the $ZnTiO_3$ phase has the Ilm structure at P < ~10 GPa, but the Pv structure at higher P (e.g., Ito and Matsui 1979; Akaogi et al. 2015) and the ZnO phase has the wurtzite structure (Wz) at P < 5 GPa but the Rs structure at higher P (e.g., Bates et al. 1962; Kusaba et al. 1999). It follows that the phase assemblage for the Zn_2TiO_4 composition at high T (1473 K for example) is presumably Zn_2TiO_4-Sp (P < ~1–4 GPa), $ZnTiO_3$-Ilm + ZnO-Wz (~1–4 < P < 5 GPa), $ZnTiO_3$-Ilm + ZnO-Rs (~5 < P < 10 GPa), and $ZnTiO_3$-Pv + ZnO-Rs (P > 10 GPa) as P increases (Table 6).

With the relevant data from Kusaba et al. (1999), Akaogi et al. (2015) and this study, the volume reduction associated with these reactions (ambient P and T) relative to the volume of the Zn_2TiO_4-Sp is calculated as ~0.52, 6.09, and 9.30 %, respectively. Furthermore, our study has suggested

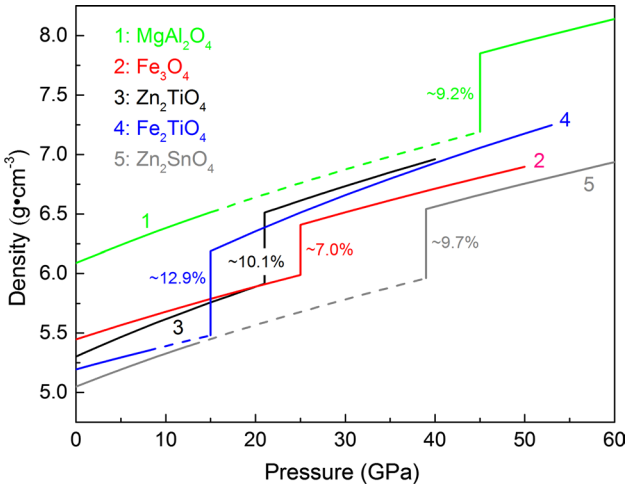

Fig. 9 Density contrasts between some spinels and their high-*P* CT phases at their phase transition pressures (ambient *T*). The *broken curves* represent the extrapolations from the stability fields of different spinels, with corresponding EoS parameters. Data sources were as follows: Zn_2TiO_4-Sp and Zn_2TiO_4-CT from this study; $MgAl_2O_4$-Sp from Finger et al. (1986) and $MgAl_2O_4$-CT from Ono et al. (2006); Fe_3O_4-Sp and Fe_3O_4-CT from Haavik et al. (2000); Fe_2TiO_4-Sp and Fe_2TiO_4-CT from Yamanaka et al. (2013); Zn_2SnO_4-Sp from Shen et al. (2009); and Zn_2SnO_4-CT from Gracia et al. (2011). Note that we did not use the new experimental result for the Fe_2TiO_4-Sp from Xiong et al. (2015) in order to achieve internal consistency

that the Zn_2TiO_4-CT is ~10.0 % denser than the Zn_2TiO_4-Sp at ambient conditions, a result certainly in sharp contrast to the ~2.1 % value claimed in Wang et al. (2002). With a volume reduction of ~0.7 % (ambient *P* and *T*), we are thus intrigued to propose the Zn_2TiO_4-CT as the immediate high-*P* phase assemblage right after the phase assemblage $ZnTiO_3$-Pv + ZnO-Rs.

This proposal seems appropriate. Figure 9 summarizes the density difference between the Sp and its corresponding post-spinel CT-type phase of variant chemical compositions, with any possible intermediate phase assemblages ignored. The density jump at this nominal phase transition varies in the range from ~7.0 to 12.9 %, and the ~10.1 % density contrast for the Zn_2TiO_4 composition (~21 GPa and room *T*) appears approximately at the middle point of this range. To critically examine this proposal, anyhow, experiments at simultaneous high-*P* and high-*T* conditions are being conducted at the High-Pressure Laboratory of Peking University.

Mg_2SiO_4-Sp and its potential post-spinel assemblages

According to the pyrolite model (Ringwood 1975), the phase olivine/wadsleyite/ringwoodite (spinel) with an approximate composition of $(Mg_{0.9}Fe_{0.1})_2SiO_4$ has a volumetric proportion up to ~60 % in the upper mantle and mantle transition zone of the Earth. Its model composition Mg_2SiO_4 therefore has been extensively explored at high *P* (e.g., Ringwood and Major 1966; Liu 1976; Ringwood and Reid 1968; Irifune and Ringwood 1987), and the discovered high-*P* phase transitions have been used to explain the major seismic discontinuities at the depths of ~410, ~520, and ~660 km (e.g., Ita and Stixrude 1992; Frost 2008). There have been controversial indications to whether the lower mantle is compositionally much similar to the upper mantle or not (e.g., Li and Zhang 2005; Ricolleau et al. 2009; Wang et al. 2015), which, however, does not expropriate the importance of the model composition Mg_2SiO_4 in the investigation of the interior structure and dynamics of the Earth.

The spinel and post-spinel phase assemblages for the Mg_2SiO_4 composition at high-*P* and high-*T* conditions soundly established so far are much comparable to those for the Zn_2TiO_4 composition deduced in this study (Table 6). The Mg_2SiO_4-Sp is stable from ~17 to 24 GPa and breaks down to $MgSiO_3$-Pv + MgO-Rs at ~24 GPa, which further changes into $MgSiO_3$-PPv + MgO-Rs at ~115 GPa (Murakami et al. 2004; Oganov and Ono 2004; Tsuchiya et al. 2004). Compared to the high-*P* phase assemblages of the Zn_2TiO_4 composition, the Mg_2SiO_4 composition does not crystallize to the phase assemblages $MgSiO_3$-Ilm + MgO-Wz and $MgSiO_3$-Ilm + MgO-Rs, but attain the extra phase assemblage $MgSiO_3$-PPv + MgO-Rs. With the unit-cell volumetric data from Wang et al. (1994; 162.28 $Å^3$ for $MgSiO_3$-Pv), Fei (1999; 74.78 $Å^3$ for MgO-Rs), Komabayashi et al. (2008; 163.81 $Å^3$ for $MgSiO_3$-PPv) and Liu et al. (2016; 526.3 $Å^3$ for Mg_2SiO_4-Sp), the volume reduction associated with these reactions (ambient *P* and *T*) relative to the volume of the Mg_2SiO_4-Sp is calculated as ~9.91 and 9.33 %, respectively. Since the magnitude of the volume reduction from the phase assemblage Mg_2SiO_4-Sp to the phase assemblage $MgSiO_3$-PPv + MgO-Rs (~9.33 %) at ambient *P* and *T* is nearly identical to that from the phase assemblage of Zn_2TiO_4-Sp to the phase assemblage $ZnTiO_3$-Pv + ZnO-Rs (~9.30 %), and since there is the phase assemblage Zn_2TiO_4-CT at higher *P* for the Zn_2TiO_4 composition, here comes a question: do the phases $MgSiO_3$-PPv and MgO-Rs recombine to form an Mg_2SiO_4-CT phase at some higher *P* for the Mg_2SiO_4 composition?

Any further high-*P* phase transition from the phase assemblage $MgSiO_3$-PPv + MgO-Rs does not seem critically important to the Earth due to the size limit of the silicate portion of this planet. It, however, may be crucial to unveil the internal dynamic processes of some extrasolar planets with masses up to 10 times that of Earth (e.g., Valencia et al. 2006; Swift et al. 2012; Wagner et al. 2012). As a matter of fact, experimental and theoretical investigations on the phase transitions of some relevant compositions such as $MgSiO_3$, MgO, and SiO_2 were recently initiated

(e.g., Umemoto et al. 2006; Tsuchiya and Tsuchiya 2011; McWilliams et al. 2012; Coppari et al. 2013). Our study here suggests that the composition Mg_2SiO_4 also deserves some attentions since there is a chance that the Mg_2SiO_4-CT may be a stable phase at very high pressures.

Acknowledgments We thank two anonymous reviewers for their constructive comments on our manuscript, and Dr T Tsuchiya for processing our paper. The high-*P* work was performed at GeoSoilEnviroCARS (Sector 13), Advanced Photon Source (APS), Argonne National Laboratory. GeoSoilEnviroCARS is supported by the National Science Foundation-Earth Sciences (EAR-1128799) and Department of Energy-GeoSciences (DE-FG02-94ER14466). Use of the COMPRES-GSECARS gas loading system was supported by COMPRES under NSF Cooperative Agreement EAR 11-57758 and by GSECARS through NSF Grant EAR-1128799 and DOE Grant DE-FG02-94ER14466. This research used resources of the Advanced Photon Source, a US Department of Energy (DOE) Office of Science User Facility operated for the DOE Office of Science by Argonne National Laboratory under Contract No. DE-AC02-06CH11357. This work is financially supported by the Natural Science Foundation of China (Grant No. 41440015 and 41273072), and by the Natural Sciences and Engineering Research Council of Canada.

References

Akaogi M, Abe K, Yusa H, Kojitani H, Mori D, Inaguma Y (2015) High-pressure phase behaviors of $ZnTiO_3$: ilmenite-perovskite transition, decomposition of perovskite into constituent oxides, and perovskite-lithium niobate transition. Phys Chem Minerals 42:421–429

Akimoto S, Syono Y (1967) High-pressure decomposition of some titanate spinels. J Chem Phys 47:1813–1817

Ali Z, Ali S, Ahmad I, Khan I, Aliabad HAR (2013) Structural and optoelectronic properties of the zinc titanate perovskite and spinel by modified Becke–Johnson potential. Phys B 420:54–57

Angel RJ (2000) Equation of state. In: Hazen RM, Downs RT (eds) High-temperature and high-pressure crystal chemistry. Reviews in mineralogy and geochemistry, vol 41. Mineralogical Society of America, Chantilly, pp 35–60

Bartram SF, Slepetys RA (1961) Compound formation and crystal structure in the system ZnO–TiO_2. J Am Ceram Soc 44:493–499

Bass JD, Liebermann RC, Weidner DJ, Finch SJ (1981) Elastic properties from acoustic and volume compression experiments. Phys Earth Planet Inter 25:140–158

Bates CH, White WB, Roy R (1962) New high-pressure polymorph of zinc oxide. Science 137:993

Bellaiche L, Vanderbilt D (2000) Virtual crystal approximation revisited: application to dielectric and piezoelectric properties of perovskites. Phys Rev B 61:7877–7882

Bertaut EF, Blum P (1956) Détermination de la structure de Ti_2CaO_4 par la Méthode Self-Consistante d'Approche Directe. Acta Crystallogr 9:121–126

Birch F (1947) Finite elastic strain of cubic crystals. Phys Rev 71:809–924

Borse PH, Cho CR, Lim KT, Hong TE, Jeong ED, Yoon JH, Yu SM, Kim HG (2012) Comparision of Zn_2TiO_4 and rutile TiO_2 photocatalysts for H_2 production under UV and near-visible light irradiation. J Ceram Process Res 13:42–46

Chaves AC, Lima SJG, Araújo RCMU, Maurera MAMA, Longo E, Pizani PS, Simões LGP, Soledade LEB, Souza AG, Santos IMG (2006) Photoluminescence in disordered Zn_2TiO_4. J Solid State Chem 179:985–992

Chen Y (2012) Dielectric properties and crystal structure of Mg_2TiO_4 ceramics substituting Mg^{2+} with Zn^{2+} and Co^{2+}. J Alloys Compd 513:481–486

Coppari F, Smith RF, Eggert JH, Wang J, Rygg JR, Lazicki A, Hawreliak JA, Collins GW, Duffy TS (2013) Experimental evidence for a phase transition in magnesium oxide at exoplanet pressures. Nat Geosci 6:926–929

de Gironcoli S, Giannozzi P, Baroni S (1991) Structure and thermodynamics of Si_xGe_{1-x} alloys from ab initio Monte Carlo simulations. Phys Rev Lett 66:2116–2119

Decker BF, Kasper JS (1957) The structure of calcium ferrite. Acta Crystallogr 10:332–337

Delamoye P, Billet Y, Michel A (1970) Etude du phenomene ordre-desordre dans les solutions dolides de l'orthotitanate de zinc. Ann Chim 5:327–334

Deng L, Liu X, Liu H, Zhang Y (2011) A first-principles study of the phase transition from Holl-I to Holl-II in the composition $KAlSi_3O_8$. Am Mineral 96:974–982

Dulin FH, Rase DE (1960) Phase equilibria in the system ZnO–TiO_2. J Am Ceram Soc 43:125–131

Errandonea D, Kumar RS, Manjón FJ, Ursaki VV, Rusu EV (2009) Post-spinel transformations and equation of state in $ZnGa_2O_4$: determination at high pressure by in situ X-ray diffraction. Phys Rev B 79:024103

Fei Y (1999) Effects of temperature and composition on the bulk modulus of (Mg, Fe)O. Am Mineral 84:272–276

Fei Y, Frost DJ, Mao HK, Prewitt CT, Häusermann D (1999) In situ structure determination of the high-pressure phase of Fe_3O_4. Am Mineral 84:203–206

Finger LW, Hazen RM, Hofmeister AM (1986) High-pressure crystal chemistry of spinel ($MgAl_2O_4$) and magnetite (Fe_3O_4): comparisons with silicate spinels. Phys Chem Minerals 13:213–220

Fleet ME, Liu X, Shieh SR (2010) Structural change in lead fluorapatite at high pressure. Phys Chem Minerals 37:1–9

Frost DJ (2008) The upper mantle and transition zone. Elements 4:171–176

Giesber HG, Pennington WT, Kolis JW (2001) Redetermination of $CaMn_2O_4$. Acta Crystallogr 57:329–330

Gracia L, Beltrán A, Andrés J (2011) A theoretical study on the pressure-induced phase transitions in the inverse spinel structure Zn_2SnO_4. J Phys Chem C 115:7740–7746

Grigoryan RA, Grigoryan LA (2001) Phase composition of Zn_2TiO_4–Zn_2ZrO_4 materials prepared by low-temperature plasma synthesis and ceramic processing. Inorg Mater 37:1061–1063

Haavik C, Stølen S, Fjellvåg H, Hanfland M, Häusermann D (2000) Equation of state of mangetite and its high-pressure modification: thermodynamics of the Fe–O system at high pressure. Am Mineral 85:514–523

Hazen RM, Yang H (1999) Effects of cation substitution and order-disorder on P–V–T equations of state of cubic spinels. Am Mineral 84:1956–1960

He Q, Liu X, Hu X, Deng L, Chen Z, Li B, Fei Y (2012) Solid solutions between lead fluorapatite and lead fluorvanadate apatite: compressibility determined by using a diamond-anvil cell coupled with synchrotron X-ray diffraction. Phys Chem Minerals 39:219–226

Heinz DL, Jeanloz R (1984) The equation of state of the gold calibration standard. J Appl Phys 55:885–893

Hill RJ, Craig JR, Gibbs GV (1979) Systematics of the spinel structure type. Phys Chem Minerals 4:317–339

Hohenberg P, Kohn W (1964) Inhomogeneous electron gas. Phys Rev 136:864–871

Holland TJB, Redfern SAT (1997) Unit cell refinement from powder diffraction data: the use of regression diagnostics. Mineral Mag 61:65–77

Irifune T, Ringwood AE (1987) Phase transformation in primitive MORB and pyrolite compositions to 25 GPa and some geophysical implications. In: Manghnani M, Syono Y (eds) High-pressure research in mineral physics. American Geophysical Union, Washington, pp 221–230

Irifune T, Fujino K, Ohtani E (1991) A new high-pressure form of $MgAl_2O_4$. Nature 349:409–411

Ita J, Stixrude L (1992) Petrology, elasticity and composition of the mantle transition zone. J Geophys Res 97:6849–6866

Ito E (1977) The absence of oxide mixture in high-pressure phases of Mg-silicates. Geophys Res Lett 4:72–74

Ito E, Matsui Y (1979) High-pressure transformations in silicates, germinates and titanates with ABO_3 stoichiometry. Phys Chem Minerals 4:265–273

Klotz S, Chervin JC, Munsch P, Le Marchand G (2009) Hydrostatic limits of 11 pressure transmitting media. J Phys D Appl Phys 42:075413

Kohn W, Sham LJ (1965) Self-consistent equations including exchange and correlation effects. Phys Rev 140:1133–1138

Komabayashi T, Hirose K, Sugimura E, Sata N, Ohishi Y, Dubrovinsky LS (2008) Simultaneous volume measurements of post-perovskite and perovskite in $MgSiO_3$ and their thermal equations of state. Earth Planet Sci Lett 265:515–524

Kresse G, Hafner J (1994) Norm-conserving and ultrasoft pseudopotentials for first-row and transition elements. J Phys Condens Matter 6:8245–8257

Kusaba K, Syono Y, Kikegawa T (1999) Phase transition of ZnO under high pressure and temperature. Proc Jpn Acad B Phys 75:1–6

Li B, Zhang J (2005) Pressure and temperature dependence of elastic wave velocity of $MgSiO_3$ perovskite and the composition of the lower mantle. Phys Earth Planet Inter 151:143–154

Liu L (1976) The post-spinel phases of forsterite. Nature 262:770–772

Liu L (1978) A new high-pressure phase of spinel. Earth Planet Sci Lett 41:398–404

Liu X, Shieh SR, Fleet ME, Zhang L, He Q (2011) Equation of state of carbonated hydroxylapatite at ambient temperature up to 10 GPa: significance of carbonate. Am Mineral 96:74–80

Liu X, Xiong Z, Chang L, He Q, Wang F, Shieh SR, Wu C, Li B, Zhang L (2016) Anhydrous ringwoodites in the mantle transition zone: their bulk modulus, solid solution behavior, compositional variation, and sound velocity feature. Solid Earth Sci 1:28–47

Lv M, Liu X, Shieh SR, Xie T, Wang F, Prescher C, Prakapenka VB (2016) Equation of state of synthetic qandilite Mg_2TiO_4 at ambient temperature. Phys Chem Minerals 43:301–306

Manik SK, Bose P, Pradhan SK (2003) Microstructure characterization and phase transformation kinetics of ball-milled prepared nanocrystalline Zn_2TiO_4 by Rietveld method. Mater Chem Phys 82:837–847

Mao HK, Bell PM, Shaner JW, Steinberg DJ (1978) Specific volume measurements of Cu, Mo, Pt, and Au and calibration of ruby R1 fluorescence pressure gauge for 0.006 to 1 Mbar. J Appl Phys 49:3276–3283

McWilliams RS, Spaulding DK, Eggert JH, Celliers PM, Hicks DG, Smith RF, Collins GW, Jeanloz R (2012) Phase transformations and metallization of magnesium oxide at high pressure and temperature. Science 338:1330–1333

Millard RL, Peterson RC, Hunter BK (1995) Study of the cubic to tetragonal transition in Mg_2TiO_4 and Zn_2TiO_4 spinels by ^{17}O MAS NMR and Rietveld refinement of X-ray diffraction data. Am Mineral 80:885–896

Miyajima N, Niwa K, Heidelbach F, Yagi T, Ohgushi K (2010) Deformation microtextures in $CaIrO_3$ post-perovskite under high stress conditions using a laser-heated diamond anvil cell. J Phys Conf Ser 215:012097

Monkhorst HJ, Pack JD (1976) Special points for Brillouin-zone integrations. Phys Rev B 13:5188–5192

Murakami M, Hirose K, Kawamura K, Sata N, Ohishi Y (2004) Post-perovskite phase transition in $MgSiO_3$. Science 304:855–858

Nestola F, Smyth JR, Parisatto M, Secco L, Princivalle F, Bruno M, Prencipe M, Dal Negro A (2009) Effects of non-stoichiometry on the spinel structure at high pressure: implications for Earth's mantle mineralogy. Geochim Cosmochim Acta 73:489–492

Nikolić MV, Obradović N, Paraskevopoulos KM, Zorba TT, Savić SM, Ristić MM (2008) Far infrared reflectance of sintered Zn_2TiO_4. J Mater Sci 43:5564–5568

Nordheim L (1931) Zur Elektronentheorie der Metalle I. Ann Phys Berlin 401:607–640

O'Neill HSC, Redfern SA, Kesson S, Short S (2003) An in situ neutron diffraction study of cation disordering in synthetic qandilite Mg_2TiO_4 at high temperatures. Am Mineral 88:860–865

Oganov AR, Ono S (2004) Theoretical and experimental evidence for a post-perovskite phase of $MgSiO_3$ in Earth's D" layer. Nature 430:445–448

Ono S, Kikegawa T, Ohishi Y (2006) The stability and compressibility of $MgAl_2O_4$ high-pressure polymorphs. Phys Chem Minerals 33:200–206

Payne MC, Teter MP, Allan DC, Arias TA, Joannopoulos JD (1992) Iterative minimization techniques for ab initio total-energy calculations: molecular dynamics and conjugate gradients. Rev Mod Phys 64:1045–1097

Perdew JP, Burke K, Ernzerhof M (1996) Generalized gradient approximation made simple. Phys Rev Lett 77:3865–3868

Prescher C, Prakapenka VB (2015) DIOPTAS: a program for reduction of two-dimensional X-ray diffraction data and data exploration. High Pressure Res 35:223–230

Ramer NJ, Rappe AM (2000) Virtual-crystal approximation that works: locating a compositional phase boundary in $Pb(Zr_{1-x}Ti_x)O_3$. Phys Rev B 62:743–746

Rankin RB, Campos A, Tian H, Siriwardane R, Roy A, Spivey JJ, Sholl DS, Johnson JK (2008) Characterization of bulk structure in zinc orthotitanate: a density functional theory and EXAFS investigation. J Am Ceram Soc 91:584–590

Ricolleau A, Fei Y, Cottrell E, Watson H, Deng L, Zhang L, Fiquet G, Auzende A-L, Roskosz M, Morard G, Prakapenka V (2009) Density profile of pyrolite under the lower mantle conditions. Geophys Res Lett 36:L06302

Ringwood AE (1975) Composition and petrology of the earth's mantle. McGraw-Hill, New York

Ringwood AE, Major A (1966) Synthesis of Mg_2SiO_4–Fe_2SiO_4 spinel solid solutions. Earth Planet Sci Lett 1:241–245

Ringwood AE, Reid AF (1968) High pressure transformations of spinels (I). Earth Planet Sci Lett 5:245–250

Rodríguez-Hernández P, Muñoz A (2014) Chapter 4 Theoretical ab initio calculations in spinels at high pressures. In: Manjon FJ, Tiginyanu I, Ursaki V (eds) Pressure-induced phase transitions in AB_2X_4 chalcogenide compounds. Springer series in materials science, vol 189. Springer, New York, pp 103–109

Santhaveesuk T, Wongratanaphisan D, Mangkorntong N, Choopun S (2008) Zn_2TiO_4 nanostructures prepared by thermal oxidation method. Adv Mater Res 55–57:641–644

Santos CL, Capistrano BJS, Vieira FTG, Santos MRC, Lima SJG, Longo E, Paskocimas CA, Souza AG, Soledade LEB, Santos IMG (2009) Structural and thermal characterization of $Zn_{2-x}Co_xTiO_4$. J Therm Anal Calorim 97:137–141

Shannon RD (1976) Revised effective ionic radii and systematic studies of interatomic distances in halides and chalcogenides. Acta Crystallogr A 32:751–756

Shen X, Shen J, You SJ, Wang LX, Tang LY, Li YC, Liu J, Yang H, Zhu K, Liu YL, Zhou WY, Jin CQ, Yu RC, Xie SS (2009) Phase

transition of Zn_2SnO_4 nanowires under high pressure. J Appl Phys 106:113523

Souza SC, Souza MAF, Lima SJG, Cassia-Santos MR, Fernandes VJ Jr, Soledade LEB, Longo E, Souza AG, Santos IMG (2005) The effects of Co, Ni and Mn on the thermal processing of Zn_2TiO_4 pigments. J Therm Anal Calorim 79:455–459

Soven P (1967) Coherent-potential model of substitutional disordered alloys. Phys Rev 156:809–813

Suito K (1972) Phase transitions of pure Mg_2SiO_4 into a spinel structure under high pressures and high temperatures. J Phys Earth 20:225–243

Swift D, Eggert J, Hicks D, Hamel S, Caspersen K, Schwegler E, Collins G, Nettelmann N, Ackland G (2012) Mass-radius relationships for exoplanets. Astrophys J 744:59

Tsuchiya T, Tsuchiya J (2011) Prediction of a hexagonal SiO_2 phase affecting stabilities of $MgSiO_3$ and $CaSiO_3$ at multimegabar pressures. Proc Natl Acad Sci USA 108:1252–1255

Tsuchiya T, Tsuchiya J, Umenoto K, Wentzcovitch RM (2004) Phase transition in $MgSiO_3$ perovskite in the Earth's lower mantle. Earth Planet Sci Lett 224:241–248

Umemoto K, Wentzcovitch RM, Allen PB (2006) Dissociation of $MgSiO_3$ in the cores of gas giants and terrestrial exoplanets. Science 311:983–986

Valencia D, O'Connell RJ, Sasselov D (2006) Internal structure of massive terrestrial planets. Icarus 181:545–554

Vanderbilt D (1990) Soft self-consistent pseudopotentials in a generalized eigenvalue formalism. Phys Rev B 41:7892–7895

Verwey EJW, Heilmann EL (1947) Physical properties and cation arrangement of oxides with spinel structures I. cation arrangement in spinels. J Chem Phys 15:174–180

Wagner FW, Tosi N, Sohl F, Rauer H, Spohn T (2012) Rocky super-Earth interiors. Structure and internal dynamics of CoRoT-7b and Kepler-10b. Astron Astrophys 541:A104

Wang Y, Weidner DJ, Liebermann RC, Zhao Y (1994) P-V-T equation of state of (Mg, Fe)SiO_3 perovskite: constraints on composition of the lower mantle. Phys Earth Planet Inter 83:13–40

Wang Z, Saxena SK, Zha CS (2002) In situ X-ray diffraction and Raman spectroscopy of pressure-induced phase transformation in spinel Zn_2TiO_4. Phys Rev B 66:024103

Wang X, Tsuchiya T, Hase A (2015) Computational support for a pyrolitic lower mantle containing ferric iron. Nat Geosci 8:556–559

Wei SH, Zhang SB (2001) First-principles study of cation distribution in eighteen closed-shell $A^{II}B_2^{III}O_4$ and $A^{IV}B_2^{II}O_4$ spinel oxides. Phys Rev B 63:045112

Xiong Z, Liu X, Shieh SR, Wang F, Wu X, Hong X, Shi Y (2015) Equation of state of a synthetic ulvöspinel, $(Fe_{1.94}Ti_{0.03})Ti_{1.00}O_{4.00}$, at ambient temperature. Phys Chem Minerals 42:171–177

Yamanaka T, Uchida A, Nakamoto Y (2008) Structural transition of post-spinel phases $CaMn_2O_4$, $CaFe_2O_4$, and $CaTi_2O_4$ under high pressures up to 80 GPa. Am Mineral 93:1874–1881

Yamanaka T, Kyono A, Nakamoto Y, Meng Y, Kharlamova S, Struzhkin VV, Mao HK (2013) High-pressure phase transitions of $Fe_{3-x}Ti_xO_4$ solid solution up to 60 GPa correlated with electronic spin transition. Am Mineral 98:736–744

Yong W, Botis S, Shieh SR, Shi W, Withers AC (2012) Pressure-induced phase transition study of magnesiochromite ($MgCr_2O_4$) by Raman spectroscopy and X-ray diffraction. Phys Earth Planet Inter 196–197:75–82

Zhang Y, Liu X, Xiong Z, Zhang Z (2016) Compressional behavior of $MgCr_2O_4$ spinel from first-principles simulation. Sci China Earth Sci 59:989–996

Zunger A, Wei SH, Ferreira LG, Bernard JE (1990) Special quasirandom structures. Phys Rev Lett 65:353–356